Journal of Alloys and Compounds 509 (2011) 6603–6608

Contents lists available at ScienceDirect

Journal of Alloys and Compounds

journal homepage: www.elsevier.com/locate/jallcom

Mechanical properties of a FeCuSiB alloy with amorphous and/or crystalline structures

Y.Y. Sun [a], M. Song [a,*], X.Z. Liao [b], Y.H. He [a]

[a] State Key Laboratory of Powder Metallurgy, Central South University, Changsha 410083, China
[b] School of Aerospace, Mechanical & Mechatronic Engineering, The University of Sydney, Sydney, NSW 2006, Australia

ARTICLE INFO

Article history:
Received 17 November 2010
Received in revised form 23 February 2011
Accepted 17 March 2011
Available online 29 March 2011

Keywords:
FeCuSiB alloy
Amorphous
Nanocrystalline
Mechanical properties

ABSTRACT

$Fe_{76.5}Cu_1Si_{13.5}B_9$ alloy rods with a diameter of 3 mm were fabricated using the copper mold suction casting method. Structural characterization revealed that different parts of the rods have different microstructures that comprise a complete amorphous structure, an amorphous-crystalline composite structure and a complete crystalline structure. Compression and nanoindentation testing showed that the hardness, strength and elastic modulus of the alloy increase with the crystalline component. High crack propagation rate and narrow shear bands contribute to the local melting and softening for the complete amorphous structure although it exhibits the lowest calculated value of the static elastic energy density.

1. Introduction

Fe-based bulk metallic glasses (BMGs) have attracted extensive interest in recent years for applications as magnetic and structural materials due to their excellent magnetic properties [1,2], high corrosion resistance [2,3] and mechanical properties [1,4]. Compared to many other BMGs, such as Zr-based or Pd-based BMGs, however, the poor glass-formation ability (GFA) substantially limits the size, and thus the applications of Fe-based BMGs. It is well known that partial substitution of Co atoms for Fe atoms in Fe-based nanocrystalline alloys increases substantially the soft magnetic properties [5,6]. However, the substitution of Co for Fe remarkably increases the cost of the materials. Recently, Ohta and Yoshizawa successfully developed nanocrystalline Fe–Cu–B and Fe–Cu–Si–B alloys with excellent soft magnetic properties through the crystallization of amorphous ribbons prepared by a single roll melt spinning process [7]. The substitution of Cu and Si for Fe plays an important role in improving the soft magnetic properties. Although previous data showed that the addition of a small amount of B or Si to the Pd–Cu–Si [8] and Fe–C–Si [9] systems can increase the GFA, the size of Fe-based BMGs with B and Si additions is still limited, which prevents many practical applications of the BMGs. It is therefore important to consider alternative Fe-based structures, e.g., BMG/nanocrystalline composites or nanocrystalline structures, with excellent magnetic and mechanical properties.

It has been well known that, in addition to alloy composition, the cooling rate from a molten alloy is also critical in producing an amorphous structure. In most situations, with the reduction of the cooling rate, the resulting structure transforms gradually from an amorphous structure to an amorphous/nanocrystalline composite and then a complete crystalline structure. This structural change unavoidably affects significantly the mechanical properties [10]. Therefore, it is expected that different parts of a Fe-based alloy rod produced by the copper mold suction casting method would have different structures and consequently different mechanical properties because of the variation in the cooling rates at the different parts of the alloy rod. In this study, we fabricated $Fe_{76.5}Cu_1Si_{13.5}B_9$ rods using the copper mold suction casting method, investigated the structures and mechanical properties at different parts of the rod, and discussed the relationship between the structures and mechanical properties of the material. The purpose of this paper was to reveal the effect of crystallization on the mechanical properties of the material.

2. Experimental

Master alloy ingots with the nominal composition of $Fe_{76.5}Cu_1Si_{13.5}B_9$ (atomic percentage) were prepared by arc melting high-purity Fe (99.9%), B (99.9%), Si (99.99%) and Cu (99.99%) in a Ti-gettered high-purity argon atmosphere. The ingots were re-melted five times and stirred by a magnetic beater to ensure its compositional homogeneity. Four cylindrical rods with a length of ~60 mm and a diameter of 3 mm were prepared by suction-casting into a water-cooled copper mold. Three parts, named P1, P2 and P3 (see Fig. 1 for details), of each rod were cut from the

* Corresponding author. Tel.: +86 731 88877880; fax: +86 731 88710855.
E-mail address: Min.Song.Th05@Alum.Dartmouth.ORG (M. Song).

0925-8388/$ – see front matter © 2011 Elsevier B.V. All rights reserved.
doi:10.1016/j.jallcom.2011.03.103

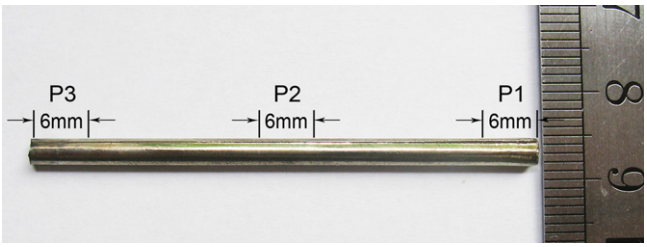

Fig. 1. An image of a typical fabricated $Fe_{76.5}Cu_1Si_{13.5}B_9$ rod and the corresponding three tested parts.

casted rods using a low speed diamond saw. The length of each part is 6 mm. Three slices with the thickness of about 0.5 mm were cut off from each part for structural characterizations and for nanoindentation testing. The rest of each part with a height of 4.5 mm was served for uniaxial compression tests. Structural characterizations were carried out using a Dmax 2500VB X-ray diffractometer (XRD) with Cu-Kα radiation, a JSM-6360LV scanning electron microscope (SEM) and a JEOL 2100F field emission transmission electron microscope (TEM). The nanoindentation testing was performed using an Ultra Nanoindentation tester with a load as high as 10 mN and a loading rate of 20 mN/min. Uniaxial compression tests were conducted using an Instron-3369 testing machine at a compression strain rate of 1×10^{-6} s^{-1}. The fracture surfaces of the specimens after compression were studied using an FEI Nano230 SEM.

3. Results and discussion

3.1. Microstructures

Fig. 2 shows the XRD patterns of P1, P2, and P3, clearly indicating that (1) P1 (the top part of a rod) has a complete amorphous structure with no detectable reflection peaks; (2) P2 is a mixture of amorphous and crystalline structures. Indexing of the diffraction peak from P2 indicates that the crystalline phase corresponds to the body-centered cubic (bcc) α-Fe (Si) [11,12]; and (3) P3 has a complete crystalline structure with bcc α-Fe (Si), body-centered tetragonal (bct) Fe_3B and bct Fe_2B phases [13,14]. The phase transformation for a whole rod can be described as: amorphous → amorphous + α-Fe → α-Fe + Fe_3B + Fe_2B.

The difference of the structures in the same casting rod is caused by the difference of the cooling rate during the casting process. The complete amorphous structure formed at a cooling rate above a critical value, below which a mixed amorphous/crystalline structure was produced. Further decrease of the cooling rate resulted in the formation of a complete crystalline structure. During the suction-casting process, the initial cooling rate was very high

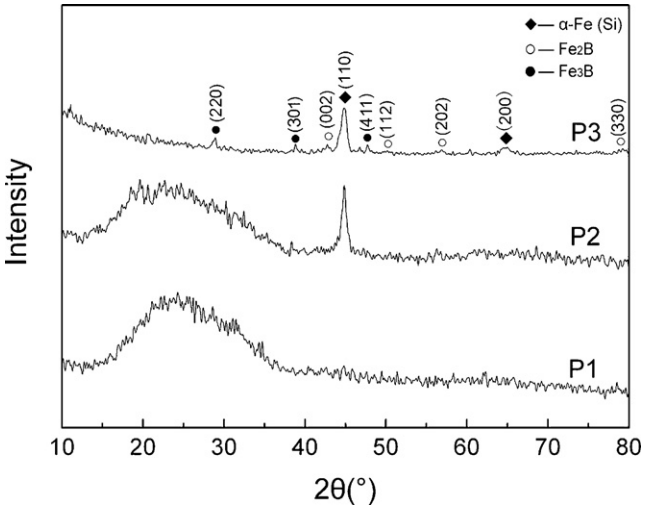

Fig. 2. XRD patterns of the three tested parts.

that formed an amorphous structure, and then the cooling rate decreases during the casting process. Four possible reasons contribute to the variation of the cooling rate during the casting process. First, the temperature of the copper mold increases as the molten liquid has been suction-casting into the mold. Second, the heat transfer is reduced because of the volume change of the molten liquid and the loss of contact between the copper mold and the undercooled liquid [15]. Third, solidification of the former molten liquid releases latent heat of fusion, which decreases the local cooling rate of the remaining molten liquid. Once some nuclei form, they act as heterogeneous nucleation centers accelerating the nucleation and the growth processes of crystalline phases. Fourth, the crystallization process modifies the composition of the remaining matrix, which also affected the GFA. From Fig. 2, it is clear that α-Fe is the starting nucleated crystalline phase in the $Fe_{76.5}Cu_1Si_{13.5}B_9$ alloy, and Fe_3B and Fe_2B are the subsequently formed crystalline phases.

Fig. 3a shows a bright-field TEM image of P1 and its corresponding selected-area electron diffraction pattern, which confirms the complete amorphous structure. A typical SEM image of P2 in Fig. 3b shows the co-existence of two phases, which, according to the XRD data in Fig. 2, are the amorphous phase and the crystalline bcc α-Fe phase. Careful examination of the SEM image shows some tiny precipitates with dark contrast and sizes of a few nanometers to tens of nanometers distributed uniformly inside the α-Fe phase. High-resolution TEM images of the α-Fe phase in P2 suggests that the precipitates are Fe_2B as the measured interplanar distances in the precipitates matched that of Fe_2B. Fig. 3c shows an example of a small sized (~5 nm) Fe_2B particle with an inter-planar distance of ~1.15 Å (note that the inter-planar distance of Fe_2B (240) plane is 1.143 Å) in the bcc α-Fe matrix. Because of the small volume fraction of the Fe_2B phase in P2 and the limited sensitivity of the XRD technique, the Fe_2B phase in P2 was not detected by XRD, as shown in Fig. 2. A bright-field TEM image of P3 and its corresponding selected-area electron diffraction (SAED) pattern, shown in Fig. 3d, suggest that P3 has a complete crystalline structure with two co-existing phases – ultrafine-grained bcc α-Fe with grain sizes of 50–200 nm and very small Fe_2B precipitates (some are indicated by arrows in Fig. 3d) distributed uniformly inside the α-Fe grains. It should be noted that no obvious diffraction spots of Fe_3B could be found in the SAED pattern. Previous studies [11,12] indicated that bcc α-Fe(Si) is the first crystallized phase during the crystallization process of amorphous Fe–Si–B alloys if the atomic concentration of B is less than 17%, followed by the crystallization of the metastable Fe_3B compound, which later decomposes to the bcc α-Fe and Fe_2B phases either at a higher temperature or during long time annealing at the same temperature. In this work, since the suction-casting process is so fast that there is no enough time for all the metastable Fe_3B particles to decompose to Fe_2B and α-Fe. Thus, some of the Fe_3B particles still exist in P3. These Fe_3B particles can be detected by XRD, since XRD examines the macro-scaled phases of the material. On the other hand, SAED is conducted in a micro-scaled area, and the selected area in Fig. 3d may not include Fe_3B particles by chance. The other possible reason might be due to the preparation of TEM specimens, which requires some time and may increase the temperature of the samples, resulting in the complete decomposition of the metastable Fe_3B phase to Fe_2B and α-Fe.

3.2. Mechanical properties

Fig. 4 shows typical compressive stress/strain curves of P1, P2, and P3 with the elastic/plastic transition points indicated by arrows. P1 exhibits fracture strength of 2575 MPa, an elastic strain of ~0.77% and a plastic strain of ~0.69%. This result is consistent with the previous report of Fe-based BMG [4] that exhibits

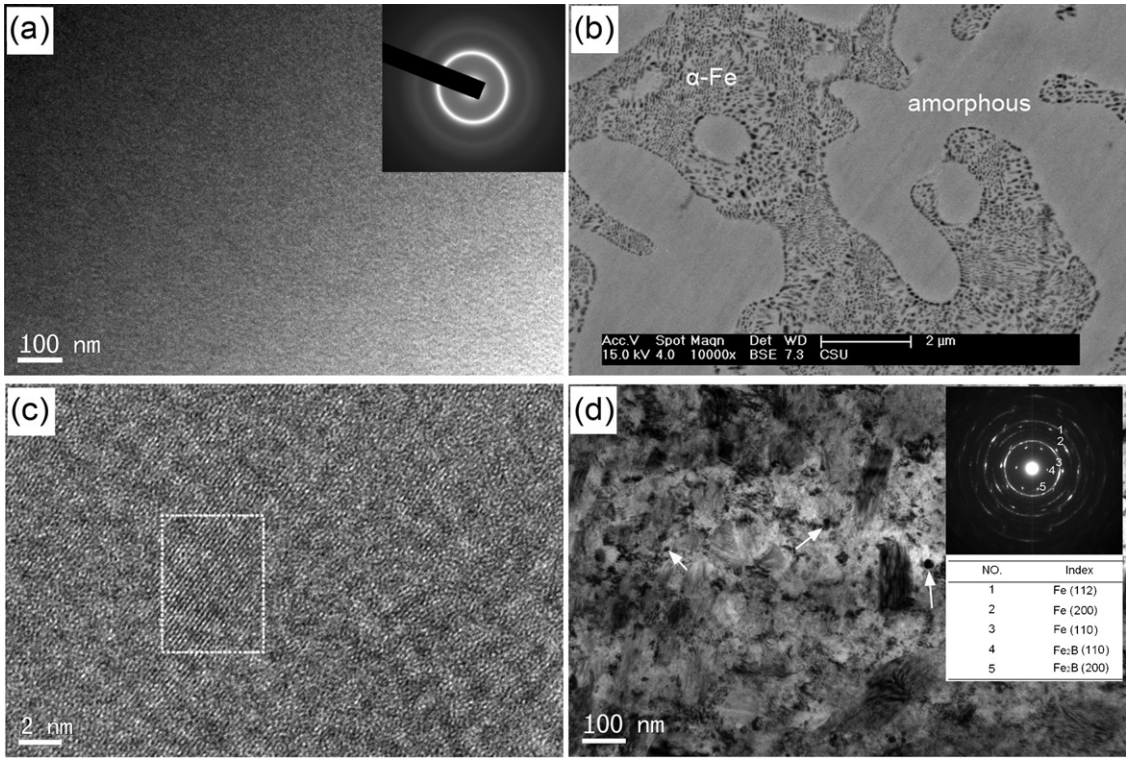

Fig. 3. (a) A TEM image and the corresponding selected area diffraction pattern of P1, showing a complete amorphous structure, (b) an SEM image of P2, (c) a high-resolution TEM image of a bcc α-Fe crystal in P2, showing a nanocrystalline Fe_2B in the α-Fe crystal, (d) a TEM image and the corresponding selected area diffraction pattern of P3, showing a complete crystalline structure.

high fracture strength in conjunction with some plastic strain. The stress/strain curves of P2 and P3 show similar features, including a small elastic deformation regime followed by some compressive plastic strain prior to failure. The compressive plastic strain for P2 and P3 is 0.94 and 1.21%, respectively. It should be noted that the generation of plastic strain for the complete amorphous structure (P1) results from the high density of the free volumes in the amorphous matrix which nucleate a large number of shear bands during compression. On the other hand, the plastic deformation for amorphous/crystalline composite structure (P2) is due to (1) the existence of a high density of free volumes in the remaining amorphous matrix, as shown in a previous study [16], (2) nano-sized Fe_2B (Fe_3B) particles uniformly distributed inside the α-Fe phase, and (3) the densely packed structure at the amorphous/crystal interface caused by the low liquid/solid interfacial energy [17]. It should be noted that the densely packed structure at the amorphous/crystal interface can help decrease the nucleation of cracks and nucleate second shear bands during deformation. It is worth to note that annealing-induced embrittlement, which has been discovered previously in Fe–Ni–Zr, Fe–Si–B and Fe–B–C systems [10,18], was not observed in this work. One important issue that should be noted is that the fracture strength increases with the volume fraction of the crystalline phases in the alloy, since the fracture strength of three parts satisfies P3 > P2 > P1.

Fig. 5 shows typical load–displacement (P–h) curves obtained by loading and unloading during nanoindentation tests. The loading part of the curves of P1, P2 and P3 are relatively smooth without

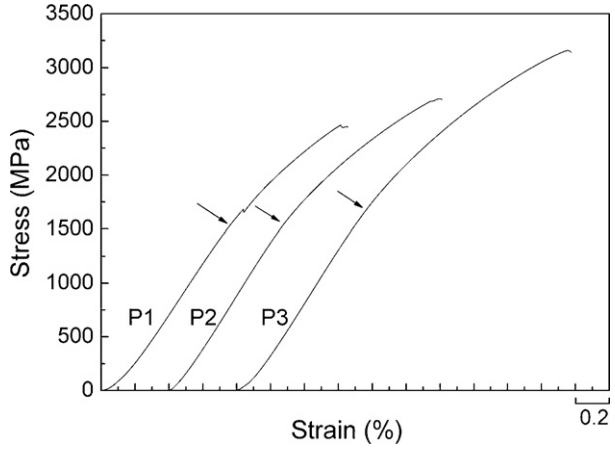

Fig. 4. Compressive stress–strain curves of P1, P2 and P3.

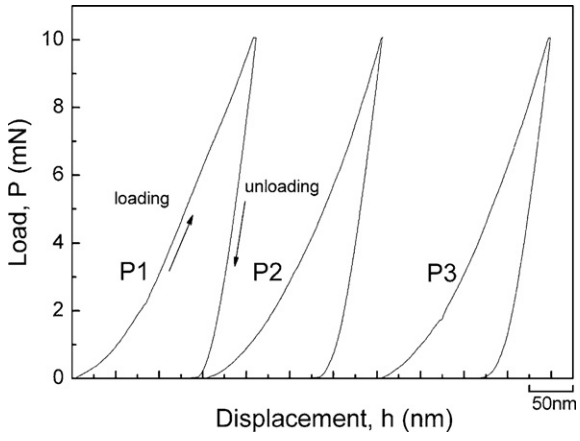

Fig. 5. Nanoindentation load–displacement curves of P1, P2 and P3. The nanoindentation tests were performed with a load as high as 10 mN and loading rate of 20 mN/min.

obvious pop-in event. Wright et al. [19,20] concluded that each pop-in corresponds to the operation of a single shear band that quickly accommodates the applied strain in BMG, and larger pop-in displacement corresponds to greater shear displacements within the shear band. The absence of pop-in for P1 and P2 is due to the small size of shear bands (less than 1 μm, see the compressive fracture surfaces in Fig. 6a and b). Another possible reason is the simultaneous operations of multiple shear bands with different orientations, which propagate to different directions from the fracture surface micrographs (see the compressive fracture surfaces in Fig. 6a and b). In addition, it is possible that the loading rate (20 mN/min) in this work was too high to generate serrated flow, as shown by Schuh and Nieh [21]. New experiments at low loading rates will be conducted to confirm this hypothesis. For complete crystalline alloys, pop-in displacement is assumed to be evidence for the activation of dislocation sources in adjacent grains [22]. Compared to the study of Yang and Vehoff [22], this study did not observe any obvious pop-in event in P3, which contains ultrafine-grained α-Fe and nano-sized Fe_2B (Fe_3B) particles. There are two possible reasons for the discrepancies between the present work and the work of Yang and Vehoff [22]. First, the plastic deformation during the indentation of our samples was accommodated by many small grains instead of the only one grain, and thus there was no enough dislocations pile up in any single grain to interact directly with the gain boundaries. Second, uniformly distributed nano-Fe_2B (Fe_3B) particles can continuously harden the ultrafine-grained α-Fe matrix, thus the pop-in phenomenon caused by dislocation/grain boundary interaction might be concealed.

The mechanical properties of P1, P2, and P3 are summarized in Table 1. It is clear that the fracture strength, elastic modulus, and hardness of the alloy increase with the volume fraction of crystals in the alloy. It should be noted that the mechanical properties of the amorphous/crystalline composite (P2) depend strongly on the crystalline bcc α-Fe phase. In the P2, the precipitation of bcc α-Fe particles results in the segregation of a large number of the other solute elements (Cu, Si, B) to the amorphous matrix [23] and might cause strengthening due to the impingement of solute diffusion profiles around the crystallites [24]. On the other hand, the homogenously distributed α-Fe particles can act as barriers against the shear displacement in the amorphous matrix due to strain accumulation around the particles during the shear-band propagation. It has been shown that P3 contains ultrafine-grained bcc α-Fe (grain size of 50–200 nm) and nano-sized Fe_2B (Fe_3B) particles distributed inside the α-Fe grains, which substantially increases the strength and ductility, compared to a single-phase structure [25]. Small grain size of the α-Fe generates a large volume fraction of the grain boundaries. Thus, the mechanical properties can be substantially improved by the inhibition of the dislocation movements due to the small grain size, large volume fraction of the boundaries and the hard Fe_2B (Fe_3B) particles.

The results of the mechanical properties in this work are consistent with the previous study [26] on a $Fe_{78}B_{13}Si_9$ alloy, since the mechanical properties of nanocrystalline $Fe_{78}B_{13}Si_9$ alloy are greater than those of the amorphous alloys. However, it should be noted that some researches indicated that the mechanical properties of some amorphous systems, including Fe–Ni–Zr [10] and Fe–C–Si [23], decrease with the increase of the volume fraction of crystalline phases.

3.3. Compressive fracture surfaces

Previous investigations showed that the fracture of BMGs usually proceeds along a shear plane declined by ~45° to the direction of the applied load under uniaxial compression test, exhibiting a well-developed vein-like pattern on the fracture surface [27]. In contrast, all the specimens in this work broke into tiny pieces with

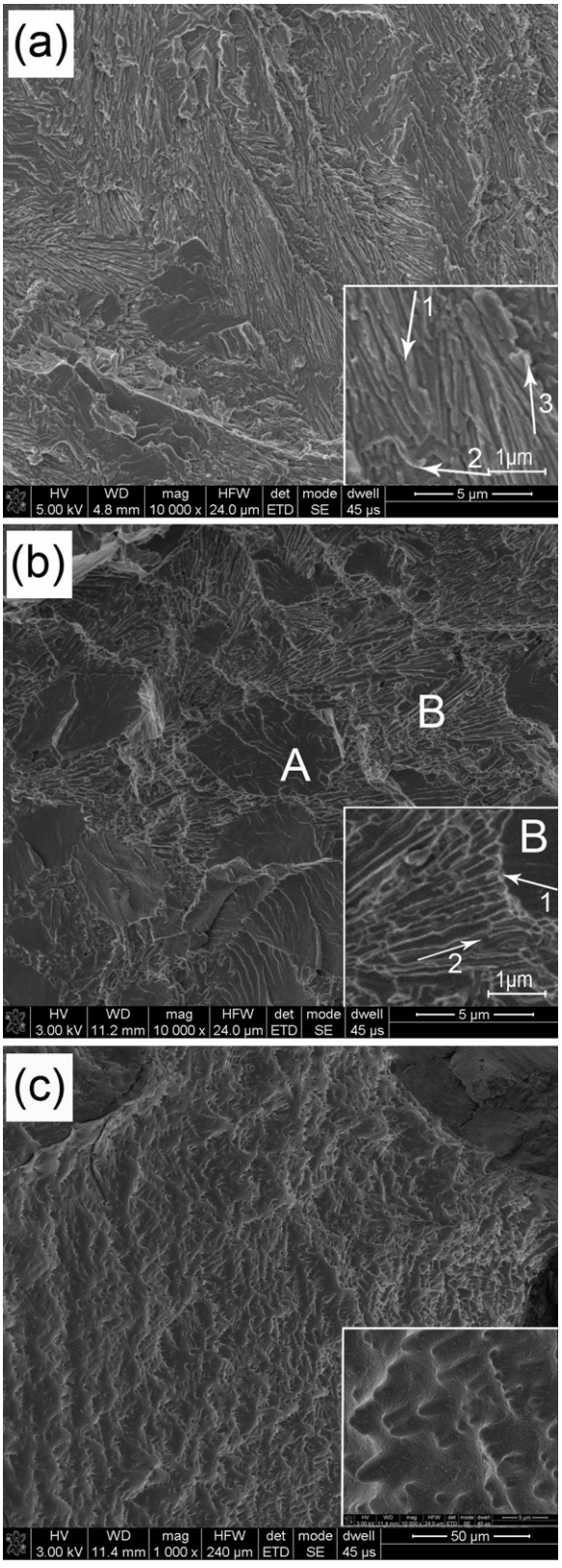

Fig. 6. SEM fracture surface images of (a) P1, (b) P2 and (c) P3 after compression.

Table 1
Mechanical properties of the tested three parts of $Fe_{76.5}Cu_1Si_{13.5}B_9$ rods.

Position	Fracture strength (MPa)	Nanoindentation		
		Vickers hardness	Hardness (GPa)	Young's modulus (GPa)
P1	2575.6 ± 111.5	932.0 ± 92.1	10.1 ± 1.0	240.9 ± 5.7
P2	2752.7 ± 312.4	1076.9 ± 165.4	11.6 ± 1.7	247.4 ± 20.0
P3	3128.7 ± 93.0	1143.9 ± 84.8	12.4 ± 0.9	263.4 ± 10.2

the size of 50 μm–1 mm, indicating a typical brittle fracture mode. This fracture mode was also observed by Chen et al. [28] and Zhang et al. [29]. Chen et al. noticed that a large number of the cracks nucleate simultaneously and propagate along variously separate planes under sufficiently high stress [28]. The intersection of the cracks with different directions results in an increased stress concentration (note that stress concentration also occurs at crack tips even without the intersection of the cracks). Final fracture would happen in an "explosion" way when the stress was released, with the specimen breaking into tiny pieces.

Fig. 6 shows the SEM micrographs of the compressive fracture surfaces of the three parts of the $Fe_{76.5}Cu_1Si_{13.5}B_9$ rods. It is clearly seen from Fig. 6a that the fracture surface of P1 consists of a high density of the small shear bands (see the inset in Fig. 6a), normally parallel to the different crack propagation directions, revealing a proper plastic flow. The fracture surface of P2 in Fig. 6b contains two different fracture zones, one of which is similar to Fig. 6a (marked as B) and is corresponding to the amorphous structure, while the other shows a typical fragmentation of the α-Fe phase (marked as A) due to the high stress concentration during deformation. The fragmentation of the α-Fe phase due to the high stress concentration decreases the plastic deformation ability, since cracks are easily nucleated. This mixed fracture mechanism is caused by the coexistence of the amorphous phase and α-Fe crystals. During compression, shear bands nucleate and propagate in the amorphous phase. Once the shear bands encounter the α-Fe crystals, their propagation is inhibited and high stress concentration is thus applied on the α-Fe crystals to cause the fragmentation of the α-Fe crystals and the cracks are nucleated. Fig. 6c shows the fracture surface of P3 after compression. The fracture surface of the ultrafine grained α-Fe phase (strengthened by nano-sized Fe_2B (Fe_3B) particles) shows obvious brittle features. The deformation mechanism of P3 is not clear at this stage. Nano-sized Fe_2B (Fe_3B) particles should have played a very important role in strengthening P3 since they can effectively pin dislocations. It should be noted that the mechanical behaviors of P3 are similar to many nanocrystalline materials such as nanocrystalline copper and nickel, for which a extremely high fracture strength and low ductility have been observed [30].

It should be noted that the fracture pattern in zone B in Fig. 6b (inset with high resolution in Fig. 6b) can be described as a meniscus pattern (see arrow 1). The formation of the meniscus pattern is caused by Taylor instability [31,32], which is associated with the tendency of a fluid meniscus with a positive pressure gradient, propagating in the direction of its convex curvature, to break up into a series of fingers. The process is considered to generate the patterns in zone B with a meniscus top and a long inserting depth as the material between the fingers necks (see arrow 2) down to failure. The fracture surface in Fig. 6a (for P1) shows similar pattern to zone B in the Fig. 6b, but the density of meniscus pattern is larger, indicating that the shear bands are narrower than those of P2. Careful measurements showed that the average width of the shear bands in P1 is 0.16 μm, while it is 0.24 μm for P2 in zone B. The meniscus top cannot be clearly seen and the ridges of the patterns are blunting (arrow 1 in the inset in Fig. 6a), which can be explained by shear-induced structural change and adiabatic heating, resulting in local softening (see arrows 2 and 3 in the inset in Fig. 6a). Previous studies [33–35] showed that the fracture of brittle materials always happens with a very high velocity, about 0.7–0.9 υ_R, with a dynamic instability (υ_R is the Rayleigh wave velocity, about 4.5 km/s). The dynamic crack propagation velocity can reach a high value for the alloy studied here. It should be noted that the driving force for crack propagation is provided by the stored elastic energy. Zhang et al. [36,37] indicated that a static elastic energy density in front of a crack tip can be expressed as $G = \sigma_s^2/2E_S$, where E_S is the static elastic modulus and σ is the static fracture strength. Based on Table 1, the static elastic energy densities were calculated to be ~13.77, ~15.31 and ~18.58 MJ m^{-3} for P1, P2 and P3, respectively. During the fracture process, although P1 has the smallest elastic energy density, the shear bands of P1 were too narrow (0.16 μm) to diffuse the excess elastic energy away in a very short time, resulting in adiabatic heating with a great temperature rising and contributing to the local melting and softening.

4. Conclusion

$Fe_{76.5}Cu_1Si_{13.5}B_9$ alloy rods have been successfully fabricated using the copper mold suction casting method. The alloy has different microstructures along the casting direction of the rods, including a complete amorphous part, an amorphous/crystalline mixture part and a complete crystalline part. The part with the complete crystalline structure shows the highest strength, hardness and elastic modulus, while the part with the complete amorphous structure presents the lowest strength, hardness and elastic modulus. The variations of the fracture surfaces of the different part of the rod can be explained by different fracture modes.

Acknowledgements

This work is supported by China–Australia Special Fund (51011120053), Australia–China Special Fund (CH090222), and National Natural Science Foundation of China (50823006, 51021063).

References

[1] A. Inoue, T. Zhang, A. Takeuchi, Appl. Phys. Lett. 71 (1997) 464–466.
[2] A. Inoue, A. Takeuchi, Mater. Trans. JIM 43 (2002) 1892–1906.
[3] S.J. Pang, T. Zhang, K. Asami, A. Inoue, Corrosion Sci. 44 (2002) 1847–1856.
[4] A. Inoue, B.L. Shen, C.T. Chang, Intermetallics 14 (2006) 936–944.
[5] M.A. Willard, D.F. Laughlin, M.E. McHenry, D. Thomas, K. Sickafus, J.O. Cross, V.G. Harris, J. Appl. Phys. 84 (1998) 6773–6777.
[6] Y. Yoshizawa, Y. Ogawa, IEEE Trans. Magn. 41 (2005) 3271–3273.
[7] M. Ohta, Y. Yoshizawa, J. Magn. Magn. Mater. 320 (2008) e750–e753.
[8] A. Inoue, T. Aoki, H. Kimura, Mater. Trans. 38 (1997) 175–178.
[9] X.M. Wang, A. Inoue, Mater. Trans. 40 (1999) 634–642.
[10] A. Inoue, H. Tomioka, T. Masumoto, J. Mater. Sci. 18 (1983) 153–160.
[11] Y. Khan, E. Kneller, M. Sostarich, Z. Metallkd. 72 (1981) 553–557.
[12] A.R. Bhatti, B. Cantor, J. Mater. Sci. 29 (1994) 816–823.
[13] L.G. Yu, X.J. Chen, K.A. Khor, G. Sundararajan, Acta Mater. 53 (2005) 2361–2368.
[14] T. Nakajima, E. Kita, H. Ino, J. Mater. Sci. 23 (1988) 1279–1288.
[15] N.H. Pryds, M. Eldrup, M. Ohnuma, A.S. Pedersen, J. Hattel, S. Linderoth, Mater. Trans. JIM 41 (2000) 1435–1442.
[16] C. Fan, A. Takeuchi, A. Inoue, Mater. Trans. JIM 40 (1999) 42–51.

[17] E.S. Machlin, Thermodynamics and Kinetics Relevant to Materials Science, Giro Press, New York, 1991, p. 125.
[18] H.S. Chen, D.E. Polk, J. Non-Cryst. Solids 15 (1974) 174–178.
[19] W.J. Wright, R. Saha, W.D. Nix, Mater. Trans. JIM 42 (2001) 642–649.
[20] C.A. Pampillo, J. Mater. Sci. 10 (1975) 1194–1227.
[21] C.A. Schuh, T.G. Nieh, Acta Mater. 51 (2003) 87–99.
[22] B. Yang, H. Vehoff, Mater. Sci. Eng. A 400–401 (2005) 467–470.
[23] A. Inoue, X.M. Wang, Acta Mater. 48 (2000) 1383–1395.
[24] Z.C. Zhong, X.Y. Jiang, A.L. Greer, Mater. Sci. Eng. A 226–228 (1997) 531–535.
[25] Y.H. Zhao, X.Z. Liao, Z. Jin, R.Z. Valiev, Y.T. Zhu, Acta Mater. 52 (2004) 4589–4599.
[26] H.Y. Tong, J.T. Wang, B.Z. Ding, H.G. Jiang, K. Lu, J. Non-Cryst. Solids 150 (1992) 444–447.
[27] A. Inoue, Acta Mater. 48 (2000) 279–306.
[28] Q.J. Chen, J. Shen, D.L. Zhang, H.B. Fan, J.F. Sun, J. Mater. Res. 22 (2007) 358–363.
[29] Z.F. Zhang, H. Zhang, B.L. Shen, A. Inoue, J. Eckert, Philos. Mag. Lett. 86 (2006) 643–650.
[30] L. Lu, Y.F. Shen, X.H. Chen, L.H. Qian, K. Lu, Science 304 (2004) 422–426.
[31] C.A. Pampillo, A.C. Reimschuessel, J. Mater. Sci. 9 (1974) 718–724.
[32] A.S. Argon, M. Salama, Mater. Sci. Eng. 23 (1976) 219–230.
[33] M.J. Buehler, H.J. Gao, Nature 439 (2006) 307–310.
[34] E. Sharon, S.P. Gross, J. Fineberg, Phys. Rev. Lett. 76 (1996) 2117–2120.
[35] T. Cramer, A. Wanner, P. Gumbsch, Z. Metallkd. 90 (1999) 675–686.
[36] Z.F. Zhang, F.F. Wu, W. Gao, J. Tan, Z.G. Wang, M. Stoica, J. Das, J. Eckert, B.L. Shen, A. Inoue, Appl. Phys. Lett. 89 (2006), 251917(1–3).
[37] J.T. Fan, Z.F. Zhang, S.X. Mao, B.L. Shen, A. Inoue, Philos. Mag. Lett. 88 (2008) 837–843.